



# Influence of post-heat treatments on the mechanical properties of CX stainless steel fabricated by selective laser melting

Cheng Chang<sup>1,2</sup>, Xingchen Yan<sup>3,4,5,\*</sup>, Rodolphe Bolot<sup>4,5</sup>, Julien Gardan<sup>1,2</sup>, Shuhong Gao<sup>4,5</sup>, Min Liu<sup>3</sup>, Hanlin Liao<sup>4,5</sup>, Mahdi Chemkhi<sup>1,2</sup>, and Sihao Deng<sup>4,5</sup>

<sup>1</sup>ICD-LASMIS, UMR CNRS 6281, University of Technology of Troyes, 12 rue Marie Curie, CS 42060, 10004 Troyes Cedex, France

<sup>2</sup>EPF, Ecole d'ingénieurs, 2 rue Fernand Sastre, Troyes, France

<sup>3</sup>National Engineering Laboratory for Modern Materials Surface Engineering Technology, The Key Lab of Guangdong for Modern Surface Engineering Technology, Guangdong Institute of New Materials, Guangzhou 510651, People's Republic of China

<sup>4</sup>ICB-PMDM, UMR 6303, CNRS, Univ. Bourgogne Franche-Comté, UBFC, 71200 Le Creusot, France

<sup>5</sup>UTBM, 90010 Belfort, France

**Received:** 11 February 2020

**Accepted:** 12 March 2020

**Published online:**

18 March 2020

© Springer Science+Business Media, LLC, part of Springer Nature 2020

## ABSTRACT

High-performance CX stainless steel was successfully manufactured using selective laser melting (SLM) technology, and different types of post-heat treatments were adopted for ameliorating the mechanical properties of as-built specimens. The microstructure evolution process (i.e., cell structures, cellular dendritic grains and blocky grains containing substructures) was explained using the rapid solidification theory after SLM. Nanoprecipitates and their hardening behavior in the SLM CX stainless steels in the as-built and solution-aged state were detected by transmission electron microscope (TEM). The results of high-resolution TEM showed that the massive needle-like nanoprecipitates with a size range of 3–25 nm (as-built sample) and 7–30 nm (solution-aged sample) were evenly distributed in the martensite matrix. In the meantime, the strengthening mechanism was analyzed and discussed. Moreover, various post-heat treatments exhibited a great influence upon the mechanical performances of the SLM CX stainless steel samples. The average micro-hardness of the SLM CX stainless steel parts was found to extremely improve from 357 HV<sub>0.2</sub> (as-built sample) to 514 HV<sub>0.2</sub> (solution-aged sample). On the contrary, the total impact energy ( $W_t$ ) of the SLM CX stainless steel parts decreased from 83.8 J in the as-built condition to 5.3 J in the solution-aged condition.

Address correspondence to E-mail: xingchen.yan@utbm.fr

## Introduction

Precipitation hardening stainless steel (PHSS), evaluated and denominated by their materials hardening ability after post-heat treatments, is a type of Fe–Cr–Ni alloy containing one or more kinds of precipitation hardening elements, e.g., Al, Ti, Mo, Cu, Nb [1, 2], etc. The high strength and hardness of the PHSS can be attained by the fine and evenly distributed intermetallic compounds [such as Ni<sub>3</sub>(Al, Ti, Mo),  $\epsilon$ -Cu, Ni<sub>3</sub>Nb, NiAl, Laves phases (AB<sub>2</sub>) and carbides] within the matrix after the precipitation hardening procedure. The brilliant mechanical performances can be achieved by a simple aging treatment at the range of 480–620 °C [3–7]. Martensitic PHSS, as a sort of steel in the PHSS family (namely, semi-austenitic PHSS, austenitic PHSS and martensitic PHSS), has captured a considerable attention in many industrial fields including aerospace [8], aircraft [9], injection molds [10], nuclear reactor [7], mechanical design [11] and so on. This type of steel has been widely utilized principally because of the unique microstructure feature, i.e., numerous intermetallic precipitates distributed in the fine martensite matrix with high-density dislocations.

Selective laser melting (SLM) technique, as a popular additive manufacturing technology for producing metallic components during these years, has been widely promoted and applied in various industrial domains [12–15]. During the metal SLM manufacturing process, firstly, a three-dimensional geometric model of a designed target part is made up of a large number of slices about 20–100  $\mu\text{m}$  provided by standard industrial STL file [16]. Then, upon high-energy laser beam irradiation driven by CAD data loaded into the 3D software, the pre-set metallic powder on the platform is selectively melted and a large number of micro-molten pools are formed subsequently. After the molten pools were rapidly solidified, the consolidated metallic material with good metallurgical interface to adjacent paths gradually forms the target component in a layer-by-layer manufacturing manner [17]. In fact, the SLM process can be regarded as a superposition of multiple micro-welding processes. Therefore, one of the vital factors to consider in the SLM fabrication procedure is weldability.

It is worth noting that martensitic PHSS is more suitable for SLM manufacturing than many types of alloy steels owing to the low carbon content ( $\omega(\text{C})$

$\leq 0.07\%$ ). Because of this characteristic, the martensite matrix formed at an extremely rapid cooling rate ( $10^3$ – $10^5$  K/s) from elevated temperature is not completely hardened [2, 18]. Moreover, driven by other unique features (such as, low crack sensitivity, good weldability and formability), martensitic PHSS with adequate hardness and strength can be perfectly fabricated by using SLM technology. As the demand and growth of the SLM continues, fabrication using the SLM with high-quality martensitic PHSS has emerged as an upcoming approach for industrial production. Murr et al. [19] reported that pre-alloyed 17-4 PH stainless steel powders were successfully manufactured using SLM technology. Compared with the original martensitic product, SLM as-fabricated 17-4 PH steel exhibited an improvement in hardness aspect from around 21 HRC to 30 HRC due to the rapid cooling affected by SLM process. According to the published document by EOS [20], additive manufactured 17-4 PH stainless steel can be hardened to 41 HRC in heat-treated condition. Sarkar et al. [21] studied that the microstructure and mechanical properties of 15-5 PH stainless steel parts built via selective laser melting process. Compared to the wrought parts, the hardness of the SLM samples can be improved from around 34 HRC to 39 HRC. In the heat-treated state, SLM 15-5 PH stainless steel can be hardened to about 43 HRC. Thus, for combining the remarkable advantage of the SLM process (i.e., rapidly fabricating hard-to-manufacture components with complicated geometry structure [22, 23]), the development a novel martensitic PHSS powder suitable for industrial applications is becoming an imminent trend.

Currently, CX stainless steel powder, a type of martensitic PHSS powder, has been announced and commercialized by EOS GmbH [24]. CX stainless steel is deemed to be a fitting material for producing molding tools and other key components that have specific demands for mechanical performances. It is well-known that post-heat treatments (such as, solution treatment [25] and aging treatment [26]) are common ways to increase the hardness of the martensitic PHSS. However, unfortunately, the increased hardness is always at the expense of toughness. To date, the microstructure evolution of the as-built sample and the effect of the different post-heat treatments upon the mechanical properties of the SLM CX stainless steel (particularly, impact toughness) have not been systematically studied.

Therefore, this paper aims to provide a detailed study into this freshly developed CX stainless steel fabricated by SLM by the means of advanced materials characterizations.

## Experimental details

### Manufacturing procedure

The CX stainless steel virgin powder (EOS GmbH Ltd., Germany) was produced by gas atomization in nitrogen atmosphere. The cross-sectional morphology of raw particles was observed by a scanning electron microscope (SEM, FEI Nova NanoSEM 450) mounted with an energy-dispersive X-ray spectroscopy (EDS), and the main elements (e.g., Fe, Cr, Ni, Al, C and the like) are distributed in the fine cellular microstructure, as shown in Fig. 1a. The nominal chemical composition of pre-alloyed CX stainless steel powder is shown in Table 1, and Fig. 1b displays that the average diameter of the powder particles is about 36.6  $\mu\text{m}$  analyzed by a Mastersizer 2000 laser diffraction particle size

machine. Besides, the flowability of the CX stainless steel powder is 32 s/50 g measured by BT-200 (Betterson Instruments Ltd., China), the apparent density is 4.11  $\text{g}/\text{cm}^3$  analyzed by BT-101 (Betterson Instruments Ltd., China), and the tap density is 4.63  $\text{g}/\text{cm}^3$  according to the tapping density test (BT-301, Betterson Instruments Ltd., China).

The laser processing parameters were screened in an EOS M290 (powder bed) system (Krailing, Germany). The SLM technological parameters are as follows: 260 W for laser power, 1060 mm/s for scanning speed, 100  $\mu\text{m}$  for hatch space and 30  $\mu\text{m}$  for layer thickness. The schematic diagram of the SLM is shown in Fig. 1c. The manufacturing procedure was realized in a working chamber with an oxygen content of less than 0.1 ppm by supplying continuous argon. A zigzag pattern with a rotation angle of 67° was chosen as laser scanning strategy. CX stainless steel blocks with dimensions of 15 mm  $\times$  15 mm  $\times$  5 mm and 55 mm  $\times$  10 mm  $\times$  10 mm were fabricated using SLM method. These samples were utilized for metallographic characterization and mechanical properties, respectively. For studying the influence of different post-heat

**Figure 1** **a** Cross-sectional microstructure of the raw powder and corresponding elements distribution mapping; **b** particle size distribution; **c** schematic diagram of the SLM processing.

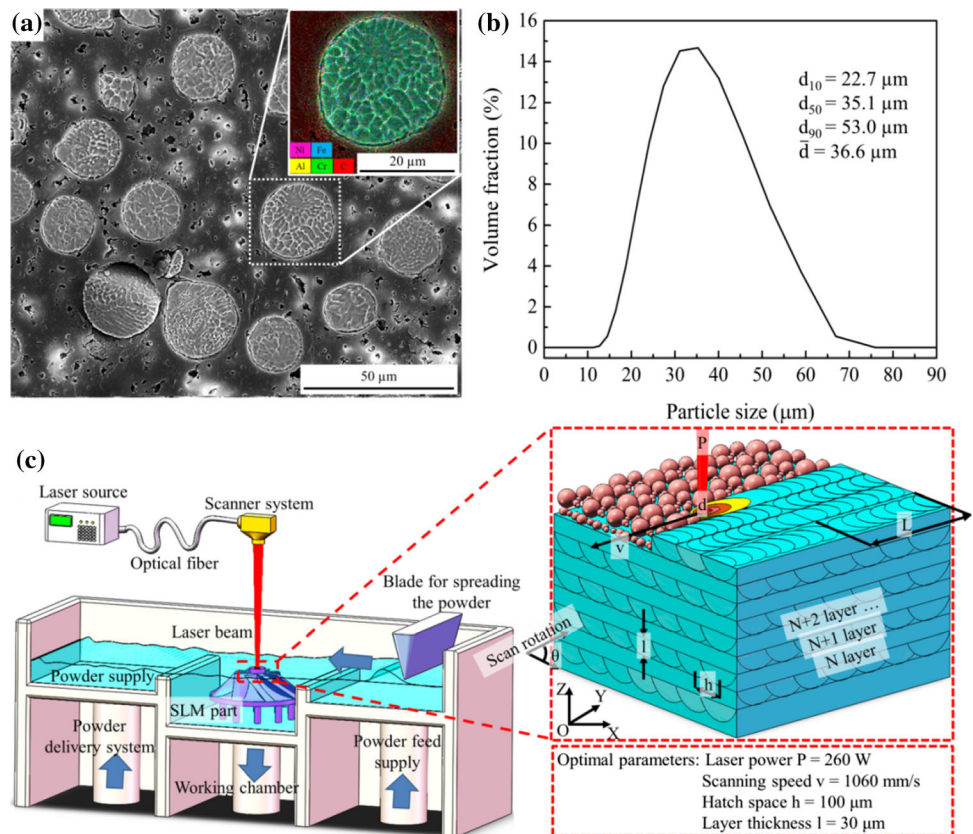


**Table 1** Nominal chemical composition of the CX stainless steel powder

Elements	Fe	Cr	Ni	Mo	Al	Mn	Si	C
Weight percentage (%)	Balance	11.00–13.00	8.40–10.00	1.10–1.70	1.20–2.00	≤ 0.40	≤ 0.40	≤ 0.05

treatments on the mechanical properties of the CX stainless steel, three different post-heat treatments are implemented on the as-built sample as follows:

1. Solution treatment at 900 °C for 1 h;
2. Aging treatment at 530 °C for 3 h;
3. An integrated heat treatment (i.e., solution treatment at 900 °C for 1 h followed by aging treatment at 530 °C for 3 h).

### Metallographic characterization

The cubic specimens (15 mm × 15 mm × 5 mm) were carefully polished by SiC grinding papers and chemically etched in Kalling's solution (i.e., 50 ml C<sub>2</sub>H<sub>5</sub>OH, 50 ml hydrochloric acid and 2.5 g CuCl<sub>2</sub>) for 30 s. Optical microscopy (OM, Leica Dmi5000a) and SEM were utilized for studying the microstructure characteristics. EDS was also applied for investigating the elements distribution. Additionally, the Titan Themis200 transmission electron microscopy (TEM) was adopted for probing the nano-sized structure and nanoprecipitates distribution after preparing the test samples, i.e., firstly cutting into thin slices, then grinding to the 20–50 μm thickness films and finally milling to 60 nm (FIB, FEI-SCIOS). Scanning transmission electron microscopy (STEM) and selected area electron diffraction (SAED) figures were also employed to determine the microstructure and nanostructure evolution after experiencing a series of heat treatments.

### Mechanical properties

The mechanical properties of the as-built samples and the post-heat-treated specimens are assessed by micro-hardness and Charpy impact tests. The Vickers micro-hardness was evaluated by a MH-5D type Vickers micro-hardness tester (Shanghai, China) under 200 g load with a dwell time of 20 s. Different areas of indentations were chosen, respectively, from the cross-sectional regions comprising the horizontal cross-sectional area (XY plane) and the vertical cross-sectional region (XZ plane), shown in Fig. 1c, and the

micro-hardness values of these two regions are the averages of 10 measurements, respectively. As shown in Fig. 2, Charpy impact parts with V-notch were manufactured in accordance to ASTM E23 standard [27]. A NI300A instrumented impact testing machine (NCS Testing Technology Ltd., China) was carried out for determining the impact toughness of the as-built samples and the different post-heat-treated samples.

## Results and discussion

### Macro-morphology characterization and microstructure evolution

The typical macro-/microstructure of the as-built sample in the transversal section plane (XY plane) vertical to the building direction and the lateral section plane (XZ plane) parallel to the building direction is shown in Fig. 3. Both in the XY plane and the XZ plane, the micro-pores and cracks are rarely distributed within the as-built sample, indicating that the successful fabrication of the completely dense SLM CX stainless steel specimens. The width of the laser scanning track can be detected as approximately 94–105 μm (Fig. 3a), which is basically equivalent to the laser spot size (100 μm). Figure 3b describes that the microstructure characteristics of the molten pools with the fish-scale morphology formed due to the extremely rapid cooling rate. The width of the molten pool (about 85–100 μm) is also substantially equal to the laser spot diameter. Besides, Fig. 3b reveals that the depth (around 28–36 μm) nearly corresponds to the powder layer thickness (30 μm), and the distance between adjacent molten pools (approximately 90–110 μm) is roughly equivalent to the hatch space (100 μm). In summary, these features clearly reflect that the as-built part with good macroscopic morphology could be successfully produced using the selected processing parameters.

Figure 3c, d shows that the microstructure of the as-built sample in different cross-sectional areas (including the XY plane and the XZ plane) is detected



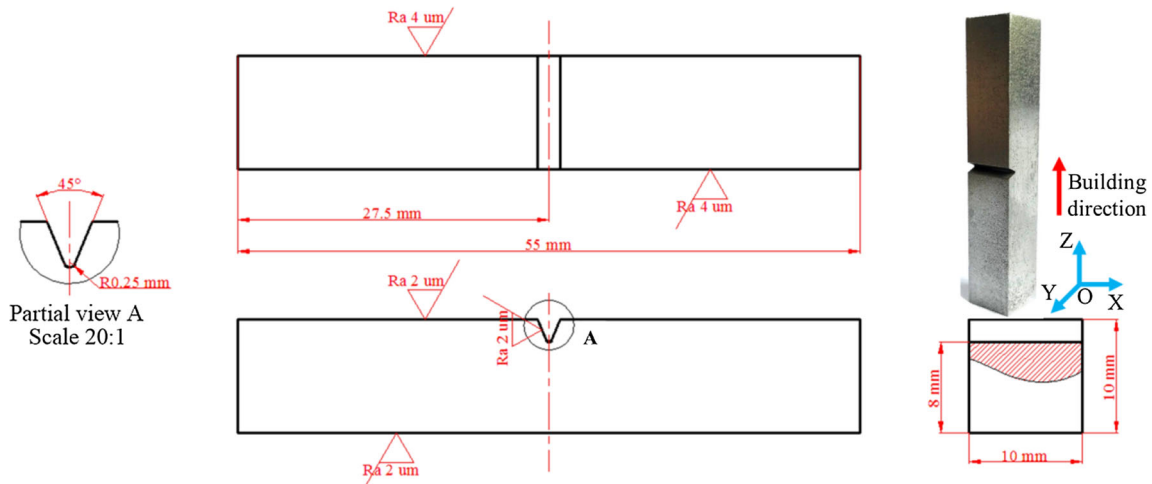
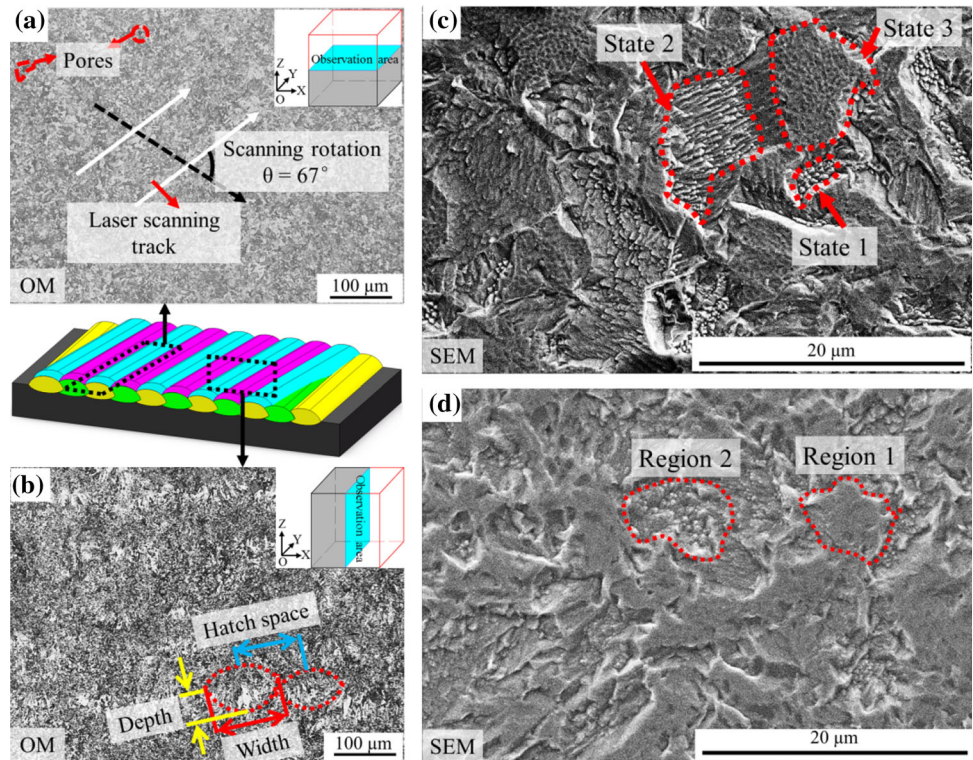


**Figure 2** Charpy V-notch impact test specimens for experimental work.

**Figure 3** Macro-/microstructure of the cross sections of the as-built sample: **a** macro-morphology of the XY plane observed using OM; **b** macro-morphology of the XZ plane observed using OM; **c** microstructure of the XY plane detected using SEM; **d** microstructure of the XZ plane detected using SEM.



using SEM, which is mainly composed of cell structures, cellular dendritic grains and blocky grains containing substructures. It is worth noting that the size of the microstructure in the XY plane (Fig. 3c) is slightly smaller than that in the XZ plane (Fig. 3d). Moreover, the substructures within the blocky grains in the XY plane also finer than that in the XZ plane. The reason for the above phenomenon can be presumed as the temper softening effect [28] and the

remelting phenomenon [29]. That is to say, during the multi-track and multilayer processing, the previous solidified layers will be rapidly remelted, which can result in a refinement of the microstructure and eliminating the preexisting defects such as pores and cracks. However, some micro-soft regions will be formed around the remelted areas, which are equivalent to being tempered. This will promote some of the solidified microstructure in the molten pool to

grow coarser. Consequently, the proportion of the coarser microstructure in the XZ plane caused by the temper softening effect was larger than that in the XY plane, while the volume fraction of the finer microstructure in the XZ plane because of the remelting phenomenon is smaller than that in the XY plane.

In order to further explore the microstructure evolution of the as-built sample after laser irradiation and rapid solidification, EDS analyses of the different microstructure (as revealed in Fig. 3d) are shown in Fig. 4. Compared to the blocky structures (region 1), the relative content of Cr element is much higher in the cell structure or the cellular dendritic grain (region 2), while the relative content of Fe element is interestingly lower.

According to the characterization results of the SEM and the EDS, the evolution process of the microstructure within the as-built sample can be illustrated as follows. Upon the basis of the constitutional supercooling theory [30, 31] and the Mullins–Sekerka (MS) instability of the planar interface [32, 33], the solid/liquid interface stability is determined by the thermal gradient, interface energy and the solute-enriched layer (i.e., a supercooled liquid region) due to solute segregation in the liquid phase at the front of the solid/liquid interface. Therefore, under rapid solidification condition, a large temperature gradient exists in a thin liquid layer at the front of the solid/liquid interface. This phenomenon will

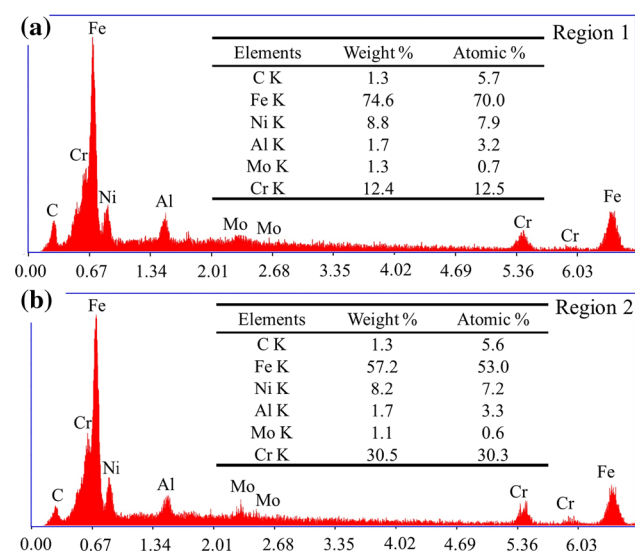


**Figure 4** Main elements distribution of the as-built part in Fig. 3d: **a** region 1; **b** region 2.

cause that the moving velocity of the solid/liquid interface is faster than the solute diffusion rate, which will further result in a non-equilibrium solidification process within the molten pool. Thus, the solute atoms (Cr atoms) enriched at the front of the solid/liquid interface are captured in the solid phase (region 2) by the rapid growth and movement of the solid/liquid interface, i.e., solute trapping phenomenon [34]. Then, the concentration of the Cr atoms near the solid–liquid interface in the solid-phase side will further increase as the molten pool solidifies. That is to say, as shown in Fig. 5, the cell structure with a relatively high content of the Cr element will nuclear and grow in the solute-enriched layer, i.e., state 1. Because the liquid phase atoms are easily stacked on the crystal faces with low solid-phase atomic density, the growth rate is high in the direction perpendicular to the crystal planes. Following the above analysis, when the solidification rate further increases, the growth direction of the cell dendrites is the vertical direction of the close-packed crystal planes. Hence, the cell structures in the as-built specimen grow in the reverse direction parallel to the heat flow to become the cellular dendritic structures, i.e., state 2. Subsequently, a plurality of cell dendritic structures having a substantially uniform growth speed gradually solidify and constitute the blocky structures containing fine substructures (region 1), i.e., state 3. Notably, the growth rate of the different types of microstructure in the molten pool is not equal due to the uneven energy distribution of the laser spot and the remelting phenomenon caused by multiple-track overlapping. As such, the final microstructure of the as-built sample includes cell structures, cellular dendritic grains and blocky structures containing substructures.

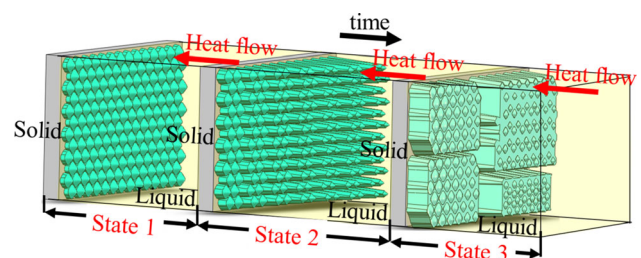


**Figure 5** Microstructure evolution process of the as-built part.

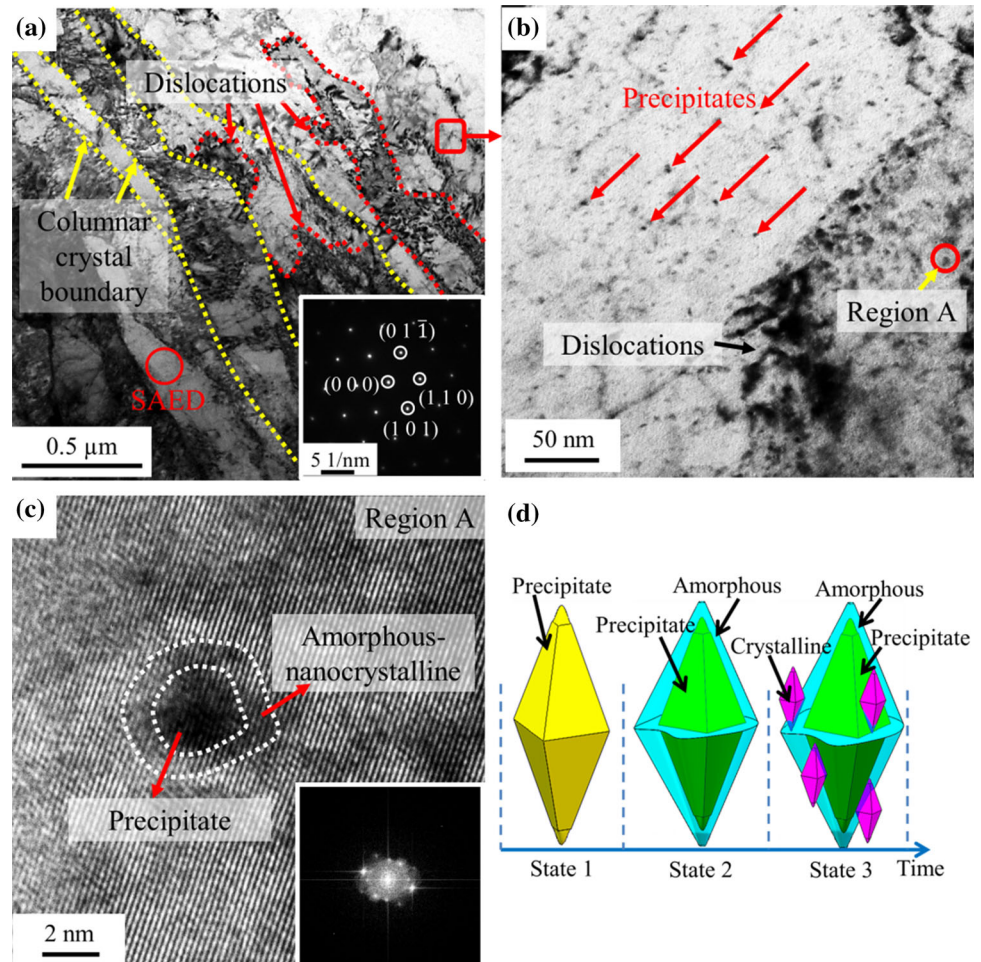


### Precipitation hardening behavior

To further investigate the nanostructure and nanoprecipitates distribution within the martensitic matrix after SLM manufacturing, the TEM observation of the as-built specimen was applied, and the results are shown in Fig. 6a–c. The typical bright-field image (BFI) displayed that the columnar crystals with a width of approximately 200 nm constituted the martensitic matrix, and this feature could be determined by the inserted corresponding SAED pattern, as shown in Fig. 6a. A large number of high-density dislocations are shown in Fig. 6a, as indicated by the red arrows. Figure 6b, the zoom-in picture of Fig. 6a, depicts that numerous fine nanoprecipitates (about 3–25 nm) are evenly distributed in the martensitic matrix, indicating that a large quantity of intermetallic compounds had formed the numerous precipitates during the SLM process. The high-resolution TEM (HRTEM) image, as shown in Fig. 6c, shows

that the amorphous–nanocrystalline composite nucleated at the surface of the nanoprecipitate. The forming process of this phenomenon can be illustrated as follows. In accordance to the heterogeneous nucleation theory [35], the non-steady amorphous–nanocrystalline composite can easily nucleate on the surfaces of the nanoprecipitates. Hence, the fine nanoprecipitates can be regarded as the heterogeneous nuclei, which were beneficial for providing a favorable crystalline surface and would further reduce the surface energy and nucleation energy. As illuminated in Fig. 6d, part of nanoprecipitates will be formed within the martensitic matrix during the SLM process, i.e., state 1. Then, non-steady amorphous structures will firstly nucleate on the surface of the nanoprecipitate, i.e., state 2. Subsequently, as the nanoprecipitates grow up, a small number of nanocrystalline structures will also nucleate on the surface of the nanoprecipitate or the amorphous phase during the heating process. After an

**Figure 6** TEM observation of the as-built sample: **a** BFI with corresponding SAED pattern; **b** zoom-in photograph of **a**; **c** HRTEM figure of precipitate and amorphous–nanocrystalline composite corresponding to the region A marked in **b**; **d** schematic diagram describing the forming process of amorphous–nanocrystalline composite marked in **c**.

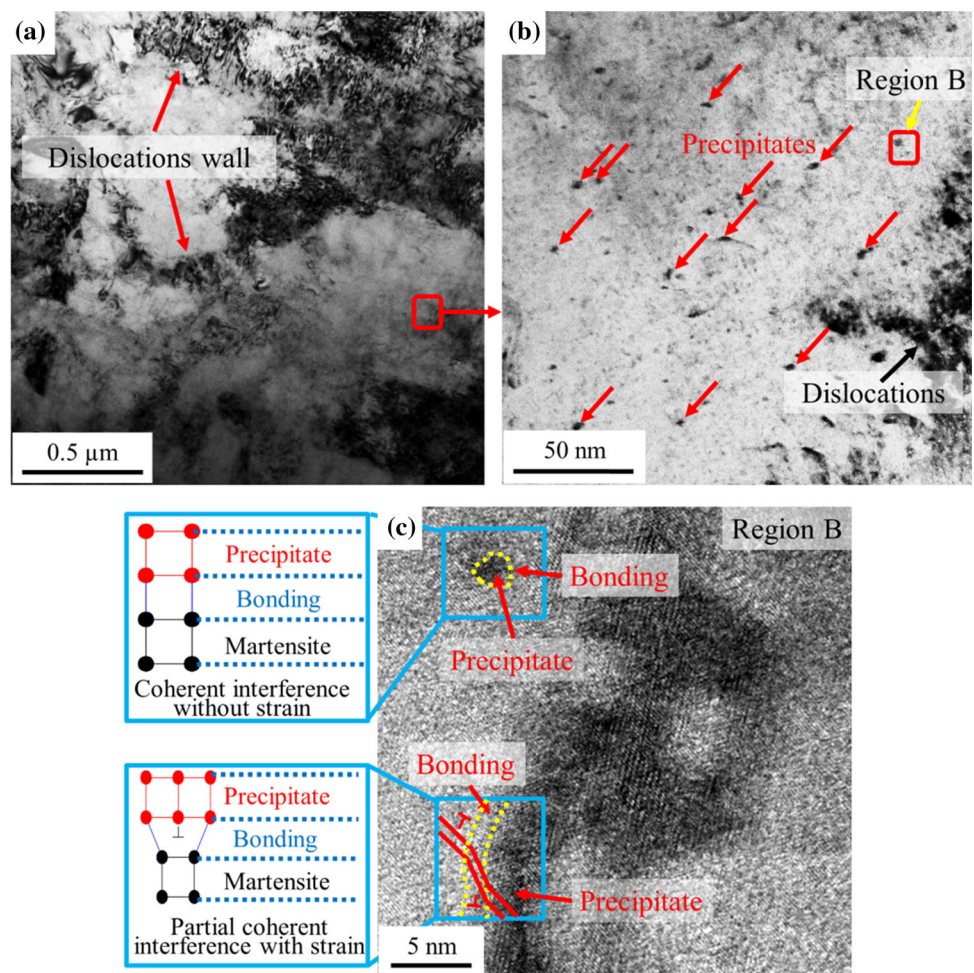


exceedingly rapid cooling rate from the elevated temperature in the molten pool, the amorphous–nanocrystalline composite will not grow up and exist within the as-built sample, just like state 3.

Because of the similar precipitates distribution characteristics after the aging treatment, only the solution-aged sample is presented in this paper. TEM analysis of the solution-aged sample is listed in Fig. 7a–c for intensive studying. Figure 7a reveals that the numerous high-density dislocation walls are still distributed near the grain boundaries after solution-aging treatment. Figure 7b, partially enlarged view in Fig. 7c, denotes that massive needle-like nanoprecipitates with sized of about 7–30 nm are distributed in the martensitic matrix. In comparison with as-built sample, the size of the nanoprecipitates formed in the solution-aged specimen is larger. Because, the time including the 1-h solution treatment and the 3-h aging treatment is sufficient for

the precipitates to nucleate at the dislocation tangles and grow up by pipe diffusion [36]. Besides, the precipitates formed in the as-built part will also experience a growth process during the solution treatment and the aging treatment. Thus, the size of the precipitates dispersed in the solution-aged sample is larger than that in the as-built specimen. As shown in Fig. 7c, when the interface between the nanoparticles and the martensitic matrix has a good matching phenomenon, the coherent interface structure without strain is formed between them. In contrast, when a misfit situation occurred at the interface between the intermetallic compounds and the martensitic matrix, the non-coherent interfaces with strain are formed. It is precisely owing to the occurrence of atomic mismatch state between the precipitates and the martensitic matrix. Therefore, the hardness of the solution-aged part will be improved, but the toughness might be decreased.

**Figure 7** TEM analysis of the solution-aged specimen: **a** BFI overview; **b** magnified view of **a**; **c** HRTEM photograph of the precipitates corresponding to the region B in **b**.





## Mechanical performances

### Micro-hardness

Figure 8 represents the average micro-hardness features of the SLM CX stainless steel samples after different post-heat treatments along the horizontal (XY plane) and vertical (XZ plane) directions. The measured average micro-hardness of the as-built sample is 357 HV<sub>0.2</sub>, and the average micro-hardness of the XY plane (366 HV<sub>0.2</sub>) is slightly higher than that of the XZ plane (348 HV<sub>0.2</sub>) due to the finer microstructure of the XY plane than that of the XZ plane. Notably, though the solution treatment reduces the hardness of the solution-treated sample (i.e., the average micro-hardness for 326 HV<sub>0.2</sub>), a complete Fe–Ni martensite structure with good deformability is obtained. Furthermore, the difference in hardness between XY plane (329 HV<sub>0.2</sub>) and XZ plane (323 HV<sub>0.2</sub>) of the solution-treated sample also become inconspicuous owing to the post-heat treatments. Additionally, the average micro-hardness of the solution-aged sample (514 HV<sub>0.2</sub>) obtained using the integrated heat treatment means is higher than that (504 HV<sub>0.2</sub>) of the aged specimen acquired by the aging treatment method. The hardness of the as-built sample is greatly improved after adopting the integrated heat treatment manner. The micro-hardness of the solution-aged part is about 144% than as-built specimen.

### Impact toughness and theoretical analysis

While employing post-heat treatments to increase the hardness of metallic material, the toughness is often

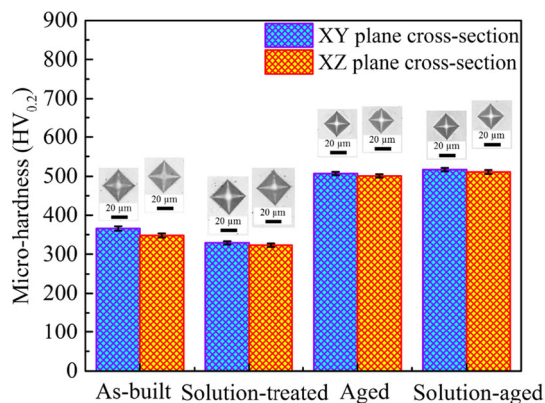


**Figure 8** Micro-hardness of the SLM CX stainless steel parts after different post-heat treatments.

sacrificed. But, the impact toughness is also a significant index to be considered in some industrial applications such as stamping or forging dies. Thus, the effect of post-heat treatments on the impact toughness of the SLM CX stainless steel should be investigated. Moreover, the as-built part treated by various post-heat treatments may exhibit different fracture features when it was subjected to a sudden and severe impact. An in-depth research into this phenomenon, however, has not been discussed and reported. Hence, the instrumented impact method was employed to measure the energy required to break the as-built sample and the various heat-treated specimens. The fracture morphology with the corresponding fracture microstructure was detected as shown in Fig. 9. As shown in Fig. 9a, a large quantity of huge and deep plastic dimples are distributed on the fracture surface of the as-built component, which indicates that a typical ductile fracture would be presented after it experiences sufficient plastic deformation. Figure 9b describes that plenty of smaller and shallower dimples and partially melted powder are dispersed on the fracture surface of the solution-treated sample. Though the solution-treated sample displays the similar ductile fracture characteristics as the as-built specimen, the dimples scattered on the fracture surface of the as-built part are still bigger and deeper than solution-treated specimen. Thereby, this phenomenon further reveals that the as-built component after SLM is better in the impact toughness owing to the finer microstructure. Figure 9c describes that other than a small quantity of little dimples, the obvious “crystalline feature” is also observed on the fracture surface of the aged sample, which proves that the fracture mechanism of the aged sample is a mixed mode of ductile and brittle fracture. Compared with the aged specimen, the characteristics of cleavage fracture (e.g., river patterns and crystalline features) can be detected on the fracture surface of the solution-aged part (Fig. 9d), which shows a transgranular brittle fracture mode. It is known that the fracture process mainly occurs in the lowest surface energy region, i.e., the cleavage surface. Thus, upon the basis of the fracture characteristics of low-carbon martensitic steel [37], its cleavage plane can be presumed to be the {110} crystal plane.

The characteristic values of forces in the impact force–displacement profiles of the SLM CX stainless steel parts in the different post-heat treatment states (Fig. 10a–d) are listed in Table 2. Because,  $F_{gy} = F_m$

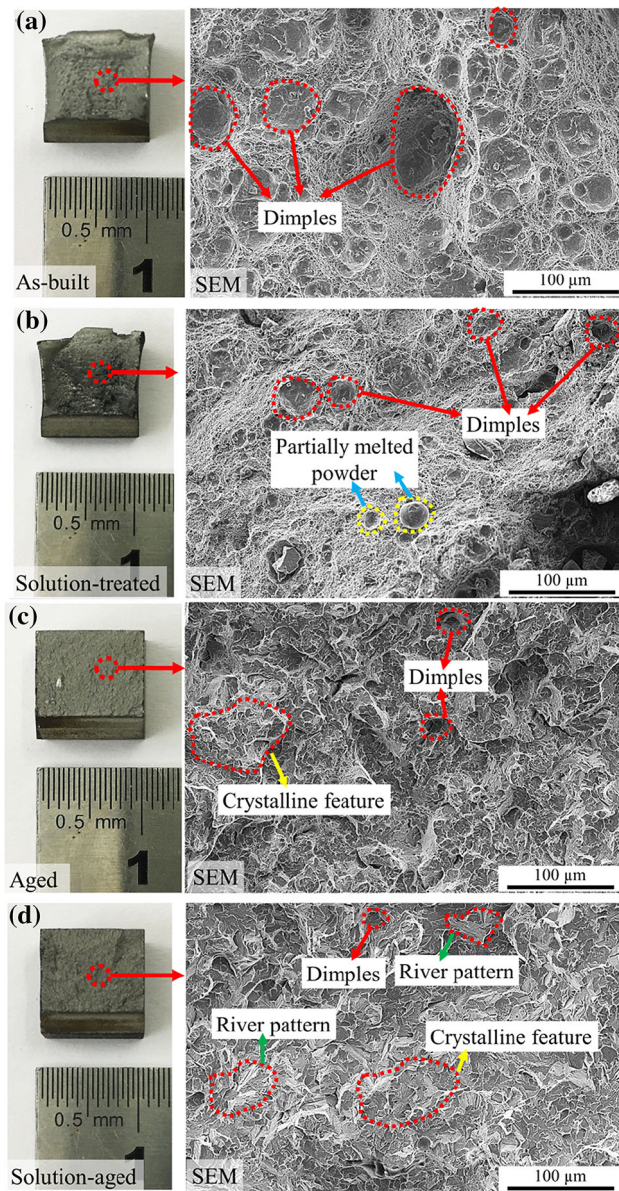


**Figure 9** Fracture morphology with the corresponding fracture microstructure observed by SEM in different post-heat treatment conditions: **a** as-built sample; **b** solution-treated sample; **c** aged-treated sample; **d** solution-aged sample.

will happen when there is a tendency to be brittle fracture, where  $F_{gy}$  and  $F_m$  are general yield force and maximum force, respectively. Therefore, in order to ensure the better evaluation of the plastic toughness after different post-heat treatments, the shear fracture percentage could be calculated by the following formula [38, 39]:

$$\% \text{Shear} = \left[ 1 - \frac{F_{iu} - F_a}{F_m} \right] \times 100$$

where  $F_{iu}$ ,  $F_a$  and  $F_m$  are characteristic points on the impact force–displacement curves.  $F_{iu}$  is force at initiation of unstable crack propagation;  $F_a$  is force at end of unstable crack propagation (arrest force). As such, the shear fracture percentage of the as-built sample, solution-treated part, aged specimen and solution-aged component can be ascertained to be 60.6%, 49.8%, 14.2% and 11.7%, respectively. Combined with the fracture mechanism of the SLM CX stainless steel samples under different heat treatment conditions, the grain size of the as-built sample is the finest due to the rapid solidification after SLM; so, the shear fracture percentage is higher than other samples. The coarse martensite microstructure will be formed in the solution-treated sample, which results in the shear fracture percentage to slightly decline than that of the as-built sample. As shown in Fig. 9c, d, the as-built part has a noticeable tendency to brittle fracture after aging treatment owing to the numerous nanoprecipitates dispersed in the martensite matrix, so their shear fracture percentage decreases sharply.

The impact energy is a significant indicator to assess the impact toughness of materials. And the characteristic values of the impact energy could be obtained from these force–displacement diagrams of the SLM CX stainless steel samples under various post-heat treatment conditions (Fig. 10), and the results are written in Table 3. The crack initiation energy ( $W_i$ ) reflects the difficulty level of crack formation and exhibits a relationship with the plastic deformation, while the crack propagation energy ( $W_p$ ) represents the crack propagation speed of the cracked specimens under the impact force, i.e., the ability to prevent crack propagation. As shown in Table 3, the  $W_i$  of the as-built sample is smaller than that of the solution-treated sample, indicating that the cracks are easily formed in the as-built sample. But interestingly, the  $W_p$  of the as-built part is higher than that of the solution-treated specimen. The reason of above phenomenon can be explained that after formation of cracks in the as-built sample, the martensite matrix with a large number of high-density dislocations can be obtained by rapid solidification process, which can hinder the further extension of the cracks. Thus, the as-built sample has a strong ability to resist crack propagation. Additionally, just like in Table 3, although the total impact energy ( $W_t$ ) of the aged sample and the solution-aged sample are almost equal, the  $W_i$  of the solution-aged sample is



**Figure 10** Impact force–displacement curves in different post-heat treatment conditions: **a** as-built sample; **b** solution-treated sample; **c** aged-treated sample; **d** solution-aged sample.

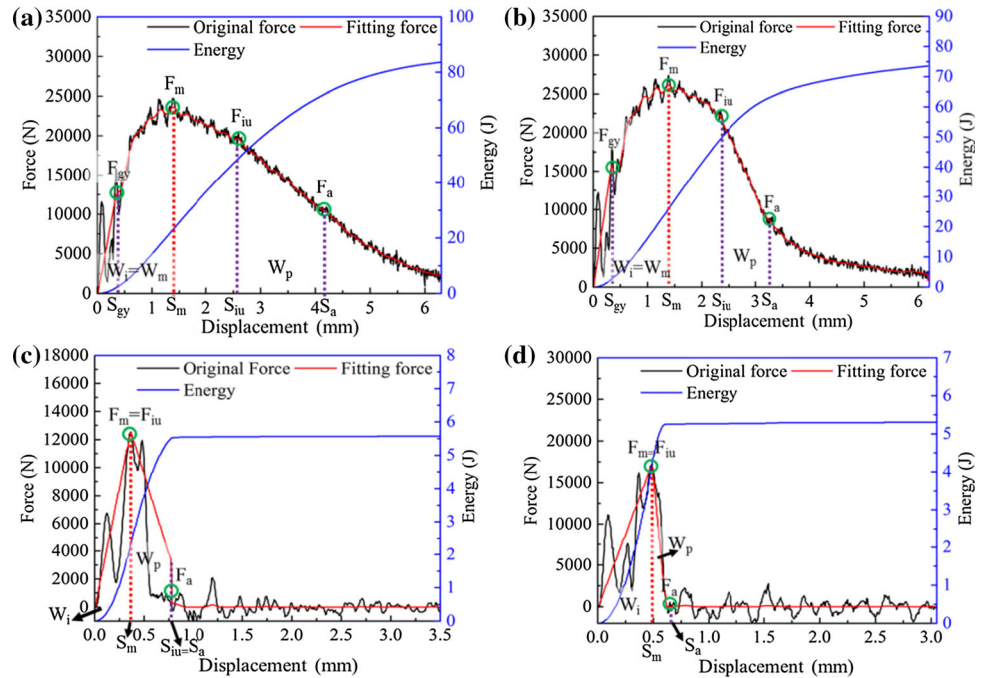


**Table 2** Characteristic values of forces in the SLM CX stainless steel impact force–displacement curves after different post-heat treatments

Sample	$F_{gy}$ (kN)	$F_m$ (kN)	$F_{iu}$ (kN)	$F_a$ (kN)	Shear fracture percentage (%)
As-built part	11.4	23.6	19.6	10.3	60.6
Solution-treated part	15.5	26.1	22.0	8.9	49.8
Aged part	/	12.6	12.6	1.8	14.2
Solution-aged part	/	17.1	17.1	2.0	11.7

**Table 3** Characteristic values of impact energy in the SLM CX stainless steel impact force–displacement diagrams after different post-heat treatments

Sample	$W_i$ (J)	$W_p$ (J)	$W_t$ (J)
As-built part	23.2	60.6	83.8
Solution-treated part	25.9	47.6	73.5
Aged part	2.3	3.2	5.5
Solution-aged part	4.2	1.1	5.3

approximately twice as large as that of the aged specimen. The reason for this phenomenon may be illustrated that part of nano-sized particles has formed in the as-built specimen, and then these nanoprecipitates will grow coarser after aging treatment. On the contrary, as for the solution-aged sample, elements will be promoted to dissolve in the martensite matrix owing to the solution treatment, and then the nanoprecipitates will be produced during the aging treatment. Hence, the size of some

nanoprecipitates in the solution-aged part may be slightly smaller than that in the aged sample. Consequently, the cracks of aged specimen will be much easier to form during the impact process. In short, although the impact toughness of the SLM CX stainless steel parts will be decreased after experiencing various post-heat treatments, the SLM CX stainless steel components are capable of obtaining a better hardness result by the post-heat treatments especially the aging process. As such, it is very vital to balance the relationship between hardness and toughness for different practical applications.

### Conclusion

In this study, a new type of PHSS, high-property CX stainless steel, was perfectly produced by utilizing the SLM technology. The microstructure evolution, precipitation hardening behavior and impact toughness properties of the SLM CX stainless steel in



different post-heat-treated states are systematically studied and main conclusions can be generalized as follows:

1. CX stainless steel sample with few defects and fine Fe–Ni martensitic microstructure can be produced employing the selective laser melting technology. Relying on the analysis of SEM and EDS, it can be speculated that the microstructure evolution process of the as-built specimen can be divided into three states: cell structure (state 1), cellular dendritic grain (state 2) and blocky grain containing substructures (state 3).
2. The martensitic matrix with the size of about 200 nm having a large number of high-density dislocations can be determined by the TEM bright-field image. The needle-shaped nanoprecipitates with a size of roughly 3–25 nm in as-built specimen can be grown to 7–30 nm approximately in the solution-aged part, which helps to increase the hardness of the SLM CX stainless steel.
3. Post-heat treatments have a good effect on improving the hardness of the SLM CX stainless steel, for example, the average micro-hardness (514 HV<sub>0.2</sub>) of the solution-aged sample is 144% as much as that of as-built specimen (357 HV<sub>0.2</sub>). By contrast, the post-heat treatments also reduce the impact toughness of the CX stainless steel, for instance, the impact energy value of the as-built specimen is reduced from 83.8 to 5.3 J owing to the integrated heat treatment. Thus, it is significant to balance the relationship between the hardness and the impact toughness for different industrial applications.

## Acknowledgements

As one of the authors, Cheng Chang is grateful for the financial support from the program of China Scholarship Council (Grant #: 201801810106). As one of the authors, Xingchen Yan, is grateful for the financial supports provided funds of Sciences Platform Environment and Capacity Building Projects of GDAS (Grant #: 2019GDASYL-0402006, 2019GDASYL-0502006, 2019GDASYL-0402004, 2018GDASCX-0402, 2018GDASCX-0111 and 2019GDASYL-0501009), Guangzhou Project of Science & Technology (Grant #: 201909010008, 201807010030),

Guangdong province Science and Technology Plan Projects (Grant #: 2017A070701027, 2017A070702016, 2014B070705007 and 2017B030314122).

## Compliance with ethical standards

**Conflict of interest** The authors declare that they have no conflict of interest.

## References

- [1] Fakić B, Čubela D (2013) Review of the Development of Research in the Design of Semi Austenitic Stainless Steel 17-7PH. *J Trends Dev Mach Assoc Technol* 17(1):57–60
- [2] Materials Information Company (1991) ASM International Handbook Committee. Properties and selection: irons steels and high performance alloys. ASM Handbook, pp 1872–1873. <https://doi.org/10.31399/asm.hb.v01.a0001046>
- [3] Guo Z, Sha W, Vaumousse D (2003) Microstructural evolution in a PH13-8 stainless steel after ageing. *Acta Mater* 51:101–116. [https://doi.org/10.1016/S1359-6454\(02\)00353-1](https://doi.org/10.1016/S1359-6454(02)00353-1)
- [4] Alafaghani A, Qattawi A, Castañón MAG (2018) Effect of manufacturing parameters on the microstructure and mechanical properties of metal laser sintering parts of precipitate hardenable metals. *Int J Adv Manuf Technol* 99:2491–2507. <https://doi.org/10.1007/s00170-018-2586-5>
- [5] Thomas G, Bell WL, Otte HM (1965) Interpretation of electron diffraction patterns from thin platelets. *Phys Status Solidi B* 12:353–366
- [6] Nakagawa H, Miyazaki T, Yokota H (2000) Effects of aging temperature on the microstructure and mechanical properties of 1.8Cu-7.3Ni-15.9Cr-1.2Mo-low C, N martensitic precipitation hardening stainless steel. *J Mater Sci* 35:2245–2253. <https://doi.org/10.1023/A:1004778910345>
- [7] Sen D, Patra AK, Mazumder S et al (2004) Carbide precipitates in solution-quenched PH13-8 Mo stainless steel: a small-angle neutron scattering investigation. *Pramana J Phys* 63:321–326. <https://doi.org/10.1007/BF02704992>
- [8] Hsiao CN, Chiou CS, Yang JR (2002) Aging reactions in a 17-4 PH stainless steel. *Mater Chem Phys* 74:134–142. [https://doi.org/10.1016/S0254-0584\(01\)00460-6](https://doi.org/10.1016/S0254-0584(01)00460-6)
- [9] Li X, Zhang J, Wang Y et al (2016) Effect of hydrogen on tensile properties and fracture behavior of PH 13-8 Mo steel. *Mater Des* 108:608–617. <https://doi.org/10.1016/j.matdes.2016.06.110>
- [10] Aizawa T, Yoshino T, Morikawa K, Yoshihara SI (2019) Microstructure of plasma nitrided AISI420 martensitic stainless steel at 673 K. *Crystals*. <https://doi.org/10.3390/cryst9020060>

- [11] Matsuzawa C, Yasuhara T, Nishizawa H, Aoki N, Takano MK (2019) Manufacturing method of mechanical component using martensitic stainless steel, rotating device, rolling bearing and rolling bearing unit. US Patent 10,494,692, 3 Dec 2019
- [12] Yan X, Chen C, Zhao R et al (2018) Selective laser melting of WC reinforced maraging steel 300: microstructure characterization and tribological performance. *Surf Coat Technol* 371:355–365. <https://doi.org/10.1016/j.surfcoat.2018.11.033>
- [13] Yan X, Yin S, Chen C et al (2018) Effect of heat treatment on the phase transformation and mechanical properties of Ti6Al4V fabricated by selective laser melting. *J Alloys Compd* 764:1056–1071. <https://doi.org/10.1016/j.jallcom.2018.06.076>
- [14] Yan X, Li Q, Yin S et al (2019) Mechanical and in vitro study of an isotropic Ti6Al4V lattice structure fabricated using selective laser melting. *J Alloys Compd* 782:209–223. <https://doi.org/10.1016/j.jallcom.2018.12.220>
- [15] Gardan J (2017) Additive manufacturing technologies: state of the art and trends. *Addit Manuf Handb Prod Dev Def Ind* 7543:149–168. <https://doi.org/10.1201/9781315119106>
- [16] Vithani K, Goyanes A, Jannin V et al (2019) An overview of 3D printing technologies for soft materials and potential opportunities for lipid-based drug delivery systems. *Pharm Res*. <https://doi.org/10.1007/s11095-018-2531-1>
- [17] Chen C, Xie Y, Yan X et al (2019) Effect of hot isostatic pressing (HIP) on microstructure and mechanical properties of Ti6Al4V alloy fabricated by cold spray additive manufacturing. *Addit Manuf* 27:595–605. <https://doi.org/10.1016/j.addma.2019.03.028>
- [18] Huang C, Yan X, Zhao L et al (2019) Ductilization of selective laser melted Ti6Al4V alloy by friction stir processing. *Mater Sci Eng, A* 755:85–96. <https://doi.org/10.1016/j.msea.2019.03.133>
- [19] Murr LE, Martinez E, Hernandez J et al (2012) Microstructures and properties of 17-4 PH stainless steel fabricated by selective laser melting. *J Mater Res Technol* 1:167–177. [https://doi.org/10.1016/S2238-7854\(12\)70029-7](https://doi.org/10.1016/S2238-7854(12)70029-7)
- [20] EOS GmbH—Electro Optical Systems (2019) EOS Stainless Steel 17-4PH. <https://www.eos.info/en>
- [21] Sarkar S, Mukherjee S, Kumar CS, Kumar Nath A (2020) Effects of heat treatment on microstructure, mechanical and corrosion properties of 15-5 PH stainless steel parts built by selective laser melting process. *J Manuf Process* 50:279–294. <https://doi.org/10.1016/j.jmapro.2019.12.048>
- [22] Yin S, Chen C, Yan X et al (2018) The influence of aging temperature and aging time on the mechanical and tribological properties of selective laser melted maraging 18Ni-300 steel. *Addit Manuf* 22:592–600. <https://doi.org/10.1016/j.addma.2018.06.005>
- [23] Palousek D, Kocica M, Pantelejev L et al (2019) SLM process parameters development of Cu-alloy Cu7.2Ni1.8-Si1Cr. *Rapid Prototype J* 25:266–276. <https://doi.org/10.1108/RPJ-06-2017-0116>
- [24] GmbH E (2019) Material data sheet—FlexLine EOS StainlessSteel CX. [https://cdn0.scrvt.com/eos/1801f2663ea474ba/efe087ff3cad/StainlessSteel-CX-M280\\_Material\\_data\\_sheet\\_09-15\\_en.pdf](https://cdn0.scrvt.com/eos/1801f2663ea474ba/efe087ff3cad/StainlessSteel-CX-M280_Material_data_sheet_09-15_en.pdf)
- [25] Harvey RF, Lake O (1972) Precipitation hardening steel
- [26] Utsunomiya T, Hoshino K, Hirotsu S (1991) Martensitic precipitation-hardenable stainless steel
- [27] ASTM E 23–12c (2013) Standard test methods for notched bar impact testing of metallic materials. Standards 1:1–25. <https://doi.org/10.1520/E0023-12C.2>
- [28] Yao C, Xu B, Huang J et al (2010) Study on the softening in overlapping zone by laser-overlapping scanning surface hardening for carbon and alloyed steel. *Opt Lasers Eng* 48:20–26. <https://doi.org/10.1016/j.optlaseng.2009.05.001>
- [29] Li Y, Gu D (2014) Thermal behavior during selective laser melting of commercially pure titanium powder: numerical simulation and experimental study. *Addit Manuf* 1:99–109. <https://doi.org/10.1016/j.addma.2014.09.001>
- [30] Tiller WA, Jackson KA, Rutter JW, Chalmers B (1953) The redistribution of solute atoms during the solidification of metals. *Acta Metall* 1:428–437
- [31] Rutter JW, Chalmers B (1953) A prismatic substructure formed during solidification of metals. *Can J Phys* 31:15–39. <https://doi.org/10.1139/p53-003>
- [32] Mullins WW, Sekerka RF (1964) Stability of a planar interface during solidification of a dilute binary alloy. *J Appl Phys* 35:444–451. <https://doi.org/10.1063/1.1713333>
- [33] Mullins WW, Sekerka RF (1963) Morphological stability of a particle growing by diffusion or heat flow. *J Appl Phys* 34:323–329. <https://doi.org/10.1063/1.1702607>
- [34] Baker JC, Gahn JW (1969) Solute trapping by rapid solidification. *Acta Metall* 17:575–578. [https://doi.org/10.1016/0001-6160\(69\)90116-3](https://doi.org/10.1016/0001-6160(69)90116-3)
- [35] Liu F, Sommer F, Bos C, Mittemeijer EJ (2007) Analysis of solid state phase transformation kinetics: models and recipes. *Int Mater Rev* 52:193–212. <https://doi.org/10.1179/174328007X160308>
- [36] Vasudevan VK, Kim SJ, Wayman CM (1990) Precipitation reactions and strengthening behavior in 18 Wt Pct nickel maraging steels. *Metall Trans A Phys Metall Mater Sci* 21:2655–2668. <https://doi.org/10.1007/BF02646061>
- [37] Morris JW (2011) On the ductile-brittle transition in lath martensitic steel. *ISIJ Int* 51:1569–1575. <https://doi.org/10.2355/isijinternational.51.1569>
- [38] American Society for Testing and Materials (2018) E2298-18: standard test method for instrumented impact testing of metallic materials. <https://doi.org/10.1520/E2298-18.2>

[39] Marietta M, Systems E (2008) Charpy impact test results on five materials and 2-mm A N D 8-mm Strikers \* portions of this document may be eligible in electronic image products. Images are produced from the best available original

**Publisher's Note** Springer Nature remains neutral with regard to jurisdictional claims in published maps and institutional affiliations.